



Tri-functional metasurface enhanced with a physically unclonable function

Soroosh Daqiqeh Rezaei^{1,2,†,‡}, Zhaogang Dong^{3,†}, Hao Wang¹, Jiahui Xu⁴, Hongtao Wang¹, Mohammad Tavakkoli Yarak⁵, Ken Choon Hwa Goh³, Wang Zhang¹, Shaban Reza Ghorbani⁶, Xiaogang Liu^{3,4}, Joel K.W. Yang^{1,3,*}

¹ Pillar of Engineering Product Development, Singapore University of Technology and Design (SUTD), 8 Somapah Road, 487372, Singapore

² Connection One, METATAG PTE. LTD., 150167, Singapore

³ Institute of Materials Research and Engineering (IMRE), A*STAR (Agency for Science, Technology and Research), 2 Fusionopolis Way, 138634, Singapore

⁴ Department of Chemistry, National University of Singapore, Singapore 117543, Singapore

⁵ School of Natural Sciences, Macquarie University, Sydney, NSW 2109, Australia

⁶ Department of Physics, Faculty of Science, Ferdowsi University of Mashhad, Mashhad, Iran

In optical anti-counterfeiting, several distinct optically variable devices (OVDs) are often concurrently employed to compensate for the insufficient security level of constituent OVDs. Alternatively, metasurfaces that exhibit multiple optical responses effectively combine multiple OVDs into one, thus significantly enhancing their security and hindering fraudulent replication. This work demonstrates the simultaneous control of three separate optical responses, *i.e.*, phase, amplitude, and luminescence, using anisotropic gap-plasmon metasurfaces. Due to the incorporated geometric anisotropy, the designed structure exhibits distinct responses under x - and y -polarized light, revealing either a color image, or a holographic projection in the far-field. Furthermore, inserting upconversion nanoparticles (UCNPs) into the dielectric gaps of the structures, the designed metasurface is able to generate a third luminescent image upon illumination with the near-infrared light. The stochastic distribution of the UCNPs constitutes a unique “fingerprint”, achieving a physically unclonable function (PUF) layer. Crucially, our triple-mode metasurface requires only readily attainable equipment such as a macro-lens/camera and a laser pointer to read most of the channels, thus paving the way towards highly secure and easy-to-authenticate metasurface-driven OVDs (mOVDs).

Keywords: Structural color; Hologram; Luminescence enhancement; Upconversion enhancement; Optical anti-counterfeiting

Introduction

Based on the unique interactions of light with nanostructures, optical metasurfaces underpin an extensive array of applications

ranging from structural color printing [1–10], next-gen displays [11–13], holography [14–19], and metalenses [20–24], to anti-counterfeiting [25–31]. Among the plethora of use cases, metasurfaces that enable manipulation of more than two types of optical properties are paramount to creating metasurface-driven optically variable devices (mOVDs) via combining several security features into one, placing a damper on the rise of counterfeit goods [32].

* Corresponding author.

E-mail addresses: Daqiqeh Rezaei, S. (szd5789@psu.edu), Yang, J.K.W. (joel_yang@sutd.edu.sg).

sg).

† Contributed equally.

‡ Present address: Department of Electrical Engineering & Materials Research Institute, The Pennsylvania State University, University Park, PA 16802, USA.

The two most common OVDs used for anti-counterfeiting are color prints and holograms [33]. Several works report on integrating these two features by simultaneous control of phase and amplitude to generate holographic and color images using metasurfaces. Such dual-mode operation is often achieved by employing Mie resonances in high refractive-index materials in combination with the geometric phase [34,35]. In this approach, the size of building blocks determines the spectral response while their orientation can tailor the designed phase distribution using a circularly polarized source [36,37]. Yet in other works, 3D printed phase plates, and waveguide modes in low-refractive-index nanopillars have been employed successfully to modulate phase and amplitude [38,39]. Another common approach integrates Fabry-Pérot color filters with other resonators to control amplitude and phase [40–42].

Alternatively, plasmonic resonators can be employed to manipulate phase and amplitude to realize mOVDs [43]. Particularly gap-plasmon resonators (GPRs) benefit from strong field confinements [44], thus achieving ultra-high-resolutions [45] not attainable by other systems. So far, GPRs have been employed to tailor various light properties such as phase [46–48], amplitude [49,50], luminescence [51], polarization [52–55], and been utilized in applications like beam steering [56–59]. Therefore, GPRs are a prime candidate to merge multiple functionalities and strengthen the security of OVDs. An ideal OVD should (1) leverage on multiple optical effects, (2) be easy to read for most modes, (3) work in reflection as most tagged assets are not transparent, (4) possess a high field of view, (5) be made from robust materials, and (6) be planar and compact.

Thus far, dual-mode mOVDs for concurrent control of phase-amplitude, or amplitude-luminescence have been reported. However, simultaneous control of phase-amplitude-

luminescence remains elusive. Here, we employ anisotropic gap-plasmon structures with integrated upconversion nanoparticles (UCNPs) to demonstrate simultaneous control of phase, amplitude, and luminescence, creating a triple-mode mOVD with overt, covert, and forensic features. The overt security feature is displayed under the white light source as a microprint, while the covert and forensic features are revealed under red and near-infrared (NIR) lasers as a hologram and luminescence image. Moreover, the stochastic distribution of UCNPs in the metasurface creates a PUF feature, rendering the mOVD physically unclonable. Not only combining multiple features drastically enhance the complexity for replication, but it also improves concealment as a single tag is used instead of multiple tags, further preventing forgery. While most of the reported works so far offer concurrent phase and amplitude control, in practice these systems are not in practice suited for easy readout due to the complicated optical setup required, *e.g.*, for circularly polarized source and analyzer. Crucially, from an application standpoint, our method enables ease of authentication using commonly available tools, *e.g.*, macro-lenses and laser pointers, while preserving covertness. In addition, the developed mOVD is fabricated from robust materials, is planar (~ 170 nm thick), and shows good angle insensitivity for the color print and the hologram, further expediting adoption.

Results and discussion

Fig. 1 schematically illustrates the tri-functional metasurface working modes. Simultaneous control of three separate optical responses, *i.e.*, phase, amplitude, and luminescence, is achieved through anisotropic gap-plasmon structures. Due to the incorporated geometric anisotropy, the design exhibits distinct responses under *x*- and *y*-polarized light, revealing either a color

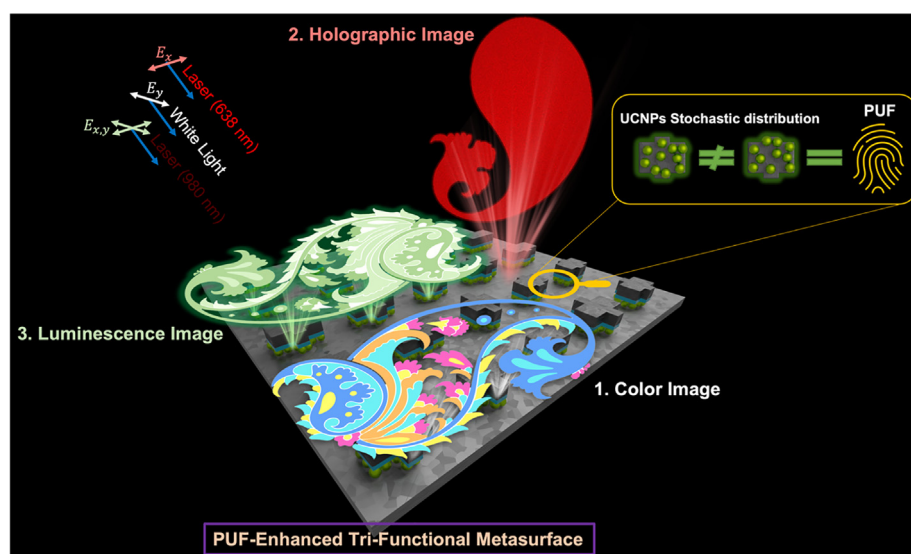


FIGURE 1

Schematic illustration of the tri-functional metasurface integrating a color print, hologram, and luminescence image by controlling amplitude, phase, and luminescence properties. The metasurface is composed of Al-based gap-plasmon nanocrosses with SiO₂ and upconversion nanoparticles (UCNPs) as the dielectric cavity. Due to the designed geometry, the structure exhibits distinct responses under *x*- and *y*-polarized light, revealing either a color image, or a holographic projection in the far-field. In addition, the metasurface is able to generate a third luminescent image in visible upon illumination with the near-infrared light. The upconversion (UC) emission from the UCNPs is enhanced by the gap-plasmon structure. Random distribution of UCNPs imparts a unique luminescence image to the metasurface, creating a physically unclonable function (PUF).

image, or a holographic projection in the far-field (Fraunhofer regime). Furthermore, inserting upconversion nanoparticles (UCNPs) into the dielectric gaps of the structures, the designed metasurface is able to generate a third luminescent image upon illumination with the near-infrared light. As the UCNPs are stochastically distributed in the gap, each metasurface holds a unique luminescence pattern resulting in a physically unclon-

able function (PUF). In the following the steps to design such metasurface is discussed.

We fabricated arrays of nanostructures, as schematically shown in Fig. 2A. Structures were fabricated by thin film deposition and patterned using electron beam lithography (EBL) as described in the Experimental section. Our proposed design relies on the anisotropy of structures with respect to x and y

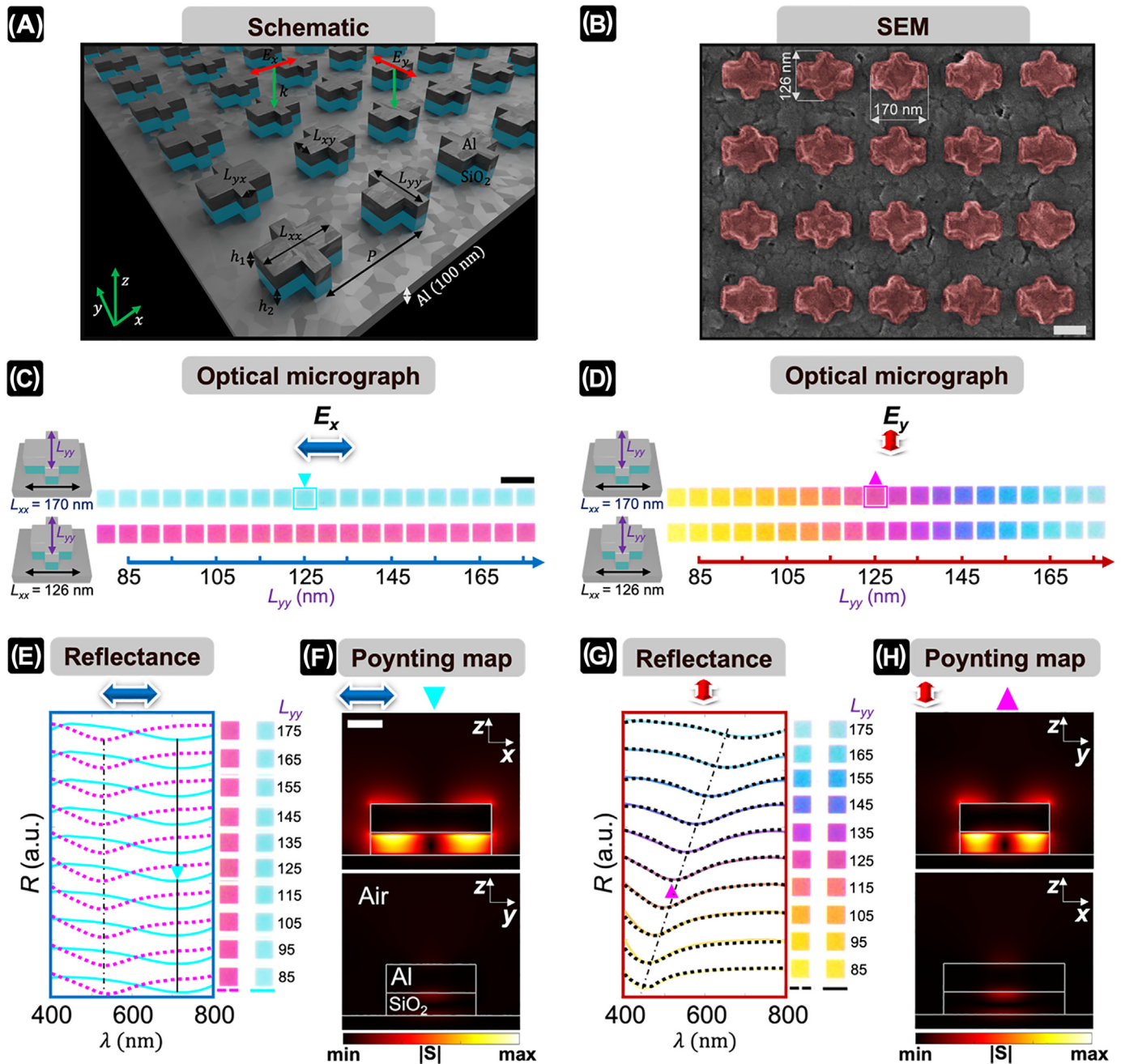


FIGURE 2

(A) Schematic of cross-shaped nanostructure array supporting gap-plasmons with armwidth $L_{xy} = 80$ nm and $L_{yx} = 40$ nm at a constant pitch $P = 250$ nm. h_1 and h_2 were set to 40 and 30 nm respectively. (B) False colorized scanning electron microscope image of the metasurface fabricated by electron beam lithography. (C) Optical micrographs of the color palette of arrays with $L_{xx} = 126$ nm and $L_{xx} = 170$ nm for $L_{yy} = 80$:5:175 nm under x-polarized and (D) y-polarized incidence. The pitch is set to $P = 250$ nm for all arrays. (E) Reflectance spectra of selected arrays with $L_{xx} = 126$ nm and $L_{xx} = 170$ nm under x-polarized light. (F) Poynting field distribution of the selected array in the x - z plane (top) and y - z plane (bottom) under x-polarized light. (G) Reflectance spectra of selected arrays with $L_{xx} = 126$ nm and $L_{xx} = 170$ nm under y-polarized light. (H) Poynting field distribution of the selected array in the y - z plane (top) and x - z plane (bottom) under y-polarized light. Scale bars in (B), (C), and (F) are 100 nm, 20 μ m, and 50 nm respectively.

polarizations. The cross-shaped gap-plasmon structure consists of a 30-nm-thick SiO₂ film sandwiched between the top 40-nm-thick Al layer and 100-nm-thick Al backreflector with an arm length of $L_{xx} = 170$ nm and $L_{yy} = 126$ nm. The scanning electron microscope (SEM) image in Fig. 2B further depicts the anisotropy of the geometry. The dimensions of the structure fabricated in this work support strong gap-plasmon resonances, similar to previous reports in the literature [60,61].

To independently control and tune the color by switching incident polarization, we fabricated the color palette in Fig. 2C with varying $L_{yy} = 80$ to 175 nm in steps of 5 nm for two arm-lengths $L_{xx} = 170$ nm and $L_{xx} = 126$ nm at constant pitch $P = 250$ nm. The armwidths L_{xy} and L_{yx} were set to 80 and 40 nm respectively to minimize the cross-talk between orthogonal polarizations while maintaining saturated colors and relatively high amplitude for a brighter hologram. The choice of geometrical parameters will be discussed in greater detail later. As can be observed under x -polarized light, with varying L_{yy} , top row remains cyan while the bottom row maintains the magenta color with small color variation in every row. The fixed color in each row albeit variation in L_{yy} is due to the constant geometrical size along x -polarization. Next, the incident light polarization is switched to y for the same color palette in Fig. 2C. In this scenario the color transitions from yellow to cyan by increasing the armlength L_{yy} , redshifting the gap-plasmon resonance with increased length along the y -axis (Fig. 2D). In this case the colors generated for any given L_{yy} look strikingly identical for $L_{xx} = 126$ and 170 nm, highlighting independent color control with polarization. This outcome showcases that the gap-plasmon resonance depends on the armlength along the polarized light rather than the arm orthogonal to the incident light polarization. In other words, the dimension along polarization dictates the resonance and the resulting color. To further investigate the optical properties of the color palette, reflectance measurements were carried out under orthogonal polarizations.

By measuring the reflectance spectra of the color palette in Fig. 2C under x -polarized light as plotted in Fig. 2E, it can be shown that in fact the resonance dips do not change for $L_{xx} = 170$ -nm and $L_{xx} = 126$ nm while L_{yy} is varied. The presence of dominant absorption dips in the reflectance spectra indicates the presence of the gap-plasmon resonance [60]. To confirm the existence of this resonance and shed light on the underlying physics inducing the absorption, the optical field distributions in the gap region are simulated at reflectance dips and plotted in orthogonal planes of the resonator.

Fig. 2F depicts the Poynting fields at the reflectance dip (highlighted with the inverse cyan triangle in Fig. 2C and E) of the color patch with $L_{xx} = 170$ nm and $L_{yy} = 125$ nm. As observed in the polarization plane, *i.e.*, top x - z , light energy is concentrated in the long arm gap with the formation of a standing wave and absorption by Al, giving rise to the reflectance dips highlighted in Fig. 2E. The confinement of light energy and the formation of a standing wave in the gap and concentrated magnetic field (see Fig. S1 for electric/magnetic-field simulations) confirm the presence of the gap-plasmon mode [62]. Conversely, the light energy concentration in the structure gap for the orthogonal plane x - y in Fig. 2F is negligible. This low energy concentration indicates that no resonance is present in the plane

of the shorter arm. However, when the polarization is switched to y , the gap-plasmon resonance is activated in the y - z plane and tuned by varying L_{yy} as elucidated in the reflectance spectra in Fig. 2G. Similar to the previous field simulation, the resonance can be observed only in the plane of polarization, *i.e.*, Fig. 2H y - z , at the highlighted reflectance dip while the orthogonal polarization plane Fig. 2H x - z shows no sign of a resonance. Therefore, by switching the incident polarization, gap-plasmon resonances can be switched on and off independently, giving rise to absorption in the visible. This effect is later employed to switch and tune the reflected amplitude and phase in orthogonal planes for color generation and holography.

To achieve the independent phase and amplitude control in orthogonal linear polarization planes, we simulated the effect of armlength variation on reflected phase as plotted in Fig. 3A. Similar to the color palette in Fig. 2C the array periodicity is set to $P = 250$ nm with $L_{yy} = 170$ nm, $L_{xy} = 80$ nm, and $L_{yx} = 40$ nm. It can be seen from the phase map that for a given wavelength, a difference of ~ 45 nm in armlength can yield a π -phase difference. This phase difference is the first step to design a binary hologram with linear polarization and constant amplitude. To find the optimum unit cell design for both color printing and holography we studied various geometrical parameters (Fig. S2-5). It should be highlighted that the effect of armlength L_{yy} is minimal on the reflected phase for x -polarization as illustrated in Fig. S6. This effect enables us to achieve low cross-talk for color printing and hologram modes of the metasurface. In fact, the design used throughout this paper is based on this optimization. For the red laser with $\lambda = 638$ nm, armlengths $L_{xx} = 126$ nm and $L_{xx} = 170$ nm yield the required π -phase separation with equal reflected amplitude according to plots in Fig. 3A and B. Similar to the independent color control shown earlier in Fig. 2C and Fig. 2D, a hologram can be encoded by setting L_{xx} to 126 nm and 170 nm to create the phase pixels and varying L_{yy} to generate different colors. With such approach a hologram can be produced under x -polarized monochromatic light while y -polarization can generate a color image, creating a dual-mode metasurface.

The color print from the dual-mode metasurface is shown in Fig. 3C. Under y -polarized white light a color print is revealed. By illuminating the metasurface with an x -polarized red laser, a hologram is projected into the far-field as captured in Fig. 3D using the optical setup schematically illustrated in Fig. S7. The SEM micrograph of the metasurface is displayed in Fig. 3E highlighting the anisotropy of the design. As can be observed from SEM micrographs, nanostructures possess rounded corners due to fabrication imperfections. Although this deviation from perfect shape induces a slight blueshift in the reflected spectra, the phase change at the red laser $\lambda = 638$ nm remains nearly unaffected (Fig. S8). Similarly, the effect of incident angle on reflected phase remains minimal, making the design robust with respect to the angle of incident (Fig. S9) and fabrication imperfections. The presented approach enables storing an independent hologram and color image in orthogonal linear polarizations. The results agree with the simulated optical micrograph and hologram in Fig. S10. Next, we attempt to utilize an additional mode, *i.e.*, illuminance, by incorporating UCNP into the dielectric gap of our design.

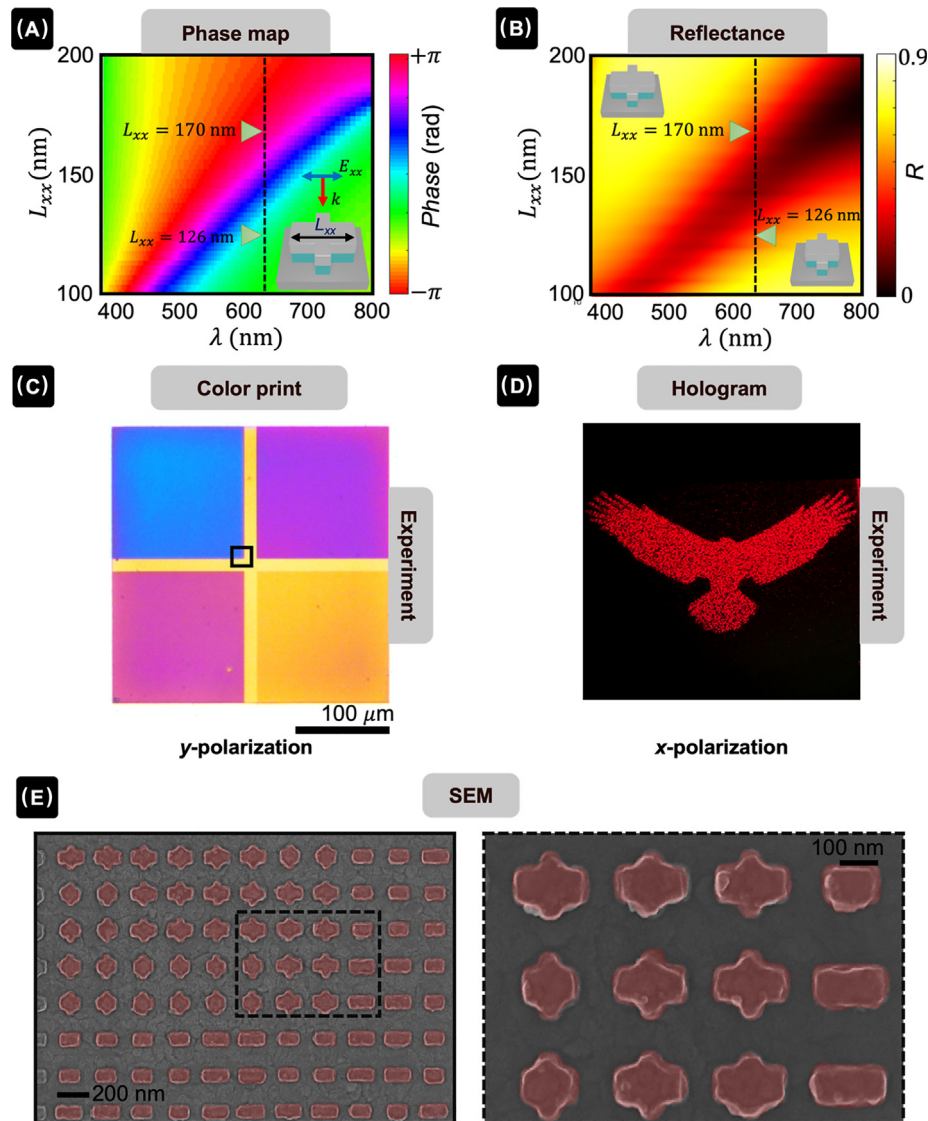


FIGURE 3

(A) Simulated reflectance phase map distribution for various armlength L_{xx} in the visible spectra under x-polarized incident light. With $P = 250$ nm, $L_{yy} = 170$ nm, $L_{xy} = 80$ nm, $L_{yx} = 40$ nm. The laser wavelength $\lambda = 638$ nm is highlighted with a dashed line. (B) Simulated reflectance map versus the armlength L_{xx} . (C) Optical micrograph of the bi-functional metasurface under y-polarized white light. (D) Experimental holographic image captured with a camera in the far-field by illuminating the bi-functional metasurface sample with an x-polarized red laser at $\lambda = 638$ nm wavelength. (E) False colored SEM image of the bi-functional metasurface sample (imaged region highlighted by a black rectangle in C) with a higher magnification inset.

The metasurface array with incorporated UCNP is schematically illustrated in Fig. 4A. The UCNP utilized here, absorb the 980 nm near-infrared (NIR) pump laser and emit through two main emission peaks in the visible spectra located at 545 and 655 nm [51]. To incorporate UCNP into the dielectric gap, after EBL and resist development steps, UCNP were spin-coated followed by electron beam evaporation (EBE) as detailed in Experimental section. Fig. 4B shows the SEM micrograph of the assembled UCNP in PMMA nanocrosses (left) and SEM of the same array after deposition of SiO_2 and Al capping layers (right). As can be seen, the assembly nearly covers the entire Al backreflector exposed through PMMA pattern. The enhanced filling factor is achieved by further optimizing the spin coating process

reported in our previous work [51]. The fabricated array is depicted under x and y-polarized illumination in Fig. 4C-D. Similar to the array in Fig. 2C, the colors can be independently controlled by switching the polarization. Notably, the colors are only slightly redshifted compared to the case without UCNP. The colors can also be observed under unpolarized source as illustrated in Fig. 4E. By illuminating the sample under near-infrared laser (NIR) excitation at 980 nm, a luminescence image of the array can be observed in Fig. 4F-H, demonstrating the presence of upconverted emission. Luminescence array colors ranges from green to blue that matches with the emission peaks of the UCNP at 545 and 655 nm. The UCNP are incorporated into the gap of the resonators including the region of enhanced electromagnetic

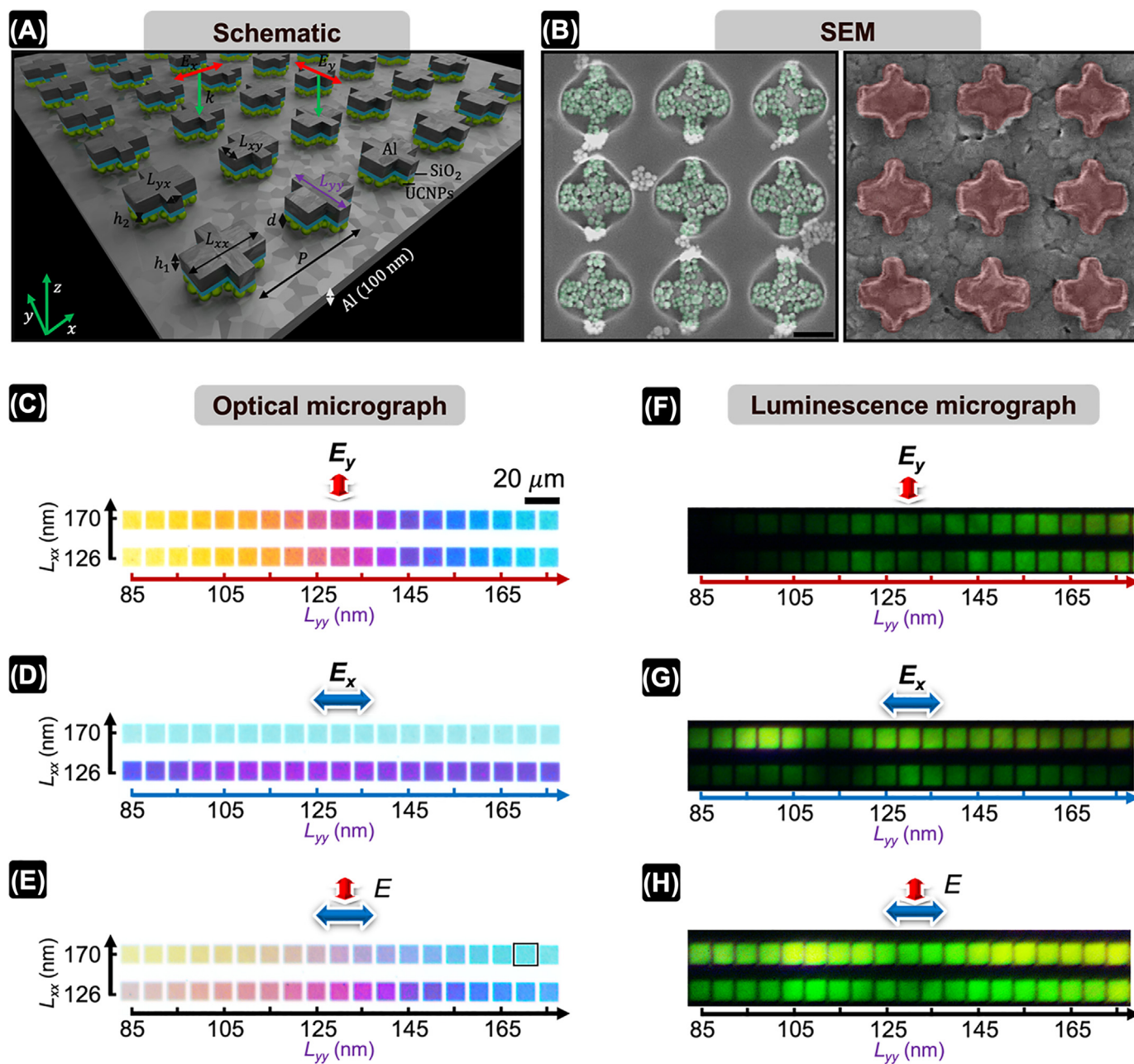


FIGURE 4

(A) Schematic of cross-shaped nanostructure array incorporating UCNPs with armwidth $L_{xy} = 80$ nm and $L_{yx} = 40$ nm at a constant pitch $P = 250$ nm. h_1 and h_2 were set to 40 and 7.5 nm respectively. The UCNPs average diameter d is 22.5 nm. (B) False colored SEM micrograph of the assembled UCNPs in PMMA nanocrosses (left) and SEM of the same array after deposition of SiO_2 and Al capping layers (right). With $P = 250$ nm, $L_{xx} = 170$ nm, $L_{yy} = 170$ nm, $L_{xy} = 80$ nm, $L_{yx} = 40$ nm. (C) Color palette of UCNPs incorporated arrays with $L_{xx} = 126$ nm and $L_{xx} = 170$ nm for $L_{yy} = 85:175$ nm under y-polarized, (D) x-polarized illumination, and (E) unpolarized white light (F) luminescence image of the same arrays under y-polarized, (G) x-polarized, and (H) unpolarized near-infrared excitation at 980 nm. The scale bar in (B) is 100 nm.

fields of the gap-plasmon mode. As a result, the UCNPs experience a large Purcell factor enhancement through plasmon-emitter coupling [51]. By tuning the size of the gap-plasmon resonators, different emission channels can be enhanced, resulting in the luminescence color tuning observed in Fig. 4H.

When the near-infrared source is γ -polarized, the patches gradually transition from dark to bright with increasing L_{yy} (Fig. 4F). The increase in brightness is consistent with the results reported in previous work [51]. with the increase in L_{yy} , the

absorption dip of the gap-plasmon resonator redshifts, approaching the pump wavelength at 980 nm. With more photons absorbed, the upconversion process is enhanced, resulting in a brighter luminescence image. It is worth noting that both rows in Fig. 4F appear nearly equally bright, as the L_{yy} is the same for both. The slightly darker patch in the center is caused by the unevenness of the laser illumination. By switching the polarization to x, the upper row appears brighter as the resonance dip for $L_{xx} = 170$ nm is closer to the pump wavelength (Fig. 4G).

Apart from the uneven illumination, the brightness is almost constant for every row as L_{xx} is constant for each row. Consequently, Fig. 4F and Fig. 4G highlight that luminescence can be controlled by polarization as well. When the array is illuminated with an unpolarized source, the brightness is considerably improved for all patches as there is no polarizer to absorb the energy (Fig. 4H), hence the upper row appears brighter. This observation can be explained if we assume that the unpolarized source is similar to the superposition of x and y -polarized sources. As the row with $L_{xx} = 170$ nm was brighter for linear polarizations, it should also be brighter for the unpolarized case. We have demonstrated independent color and phase control by switching polarization in addition to up-conversion illuminance. Based on results above, we next show how these modes can be employed in a single metasurface.

The metasurface in Fig. 5A is fabricated by incorporating UCNPs into the gap. Similar to the arrays in Fig. 4, armwidths are set to $L_{xy} = 80$ nm and $L_{yx} = 40$ nm at a constant pitch of $P = 250$ nm. Armlength L_{xx} is set to either $L_{xx} = 126$ nm or $L_{xx} = 170$ nm to generate the binary hologram using x -polarized laser, while armlength L_{yy} is varied from 80 to 175 nm for color generation under y -polarized white light. h_1 and h_2 were set to 40 and 7.5 nm respectively. As can be observed, a color image appears under y -polarized white light, while pumping an NIR laser and illuminating with an x -polarized red laser produces a luminescence image and a far-field hologram, respectively (Fig. 5B and Fig. 5C). The experimental results are in good agreement with simulations in Fig. S11. Notably, different luminescence images can be generated under

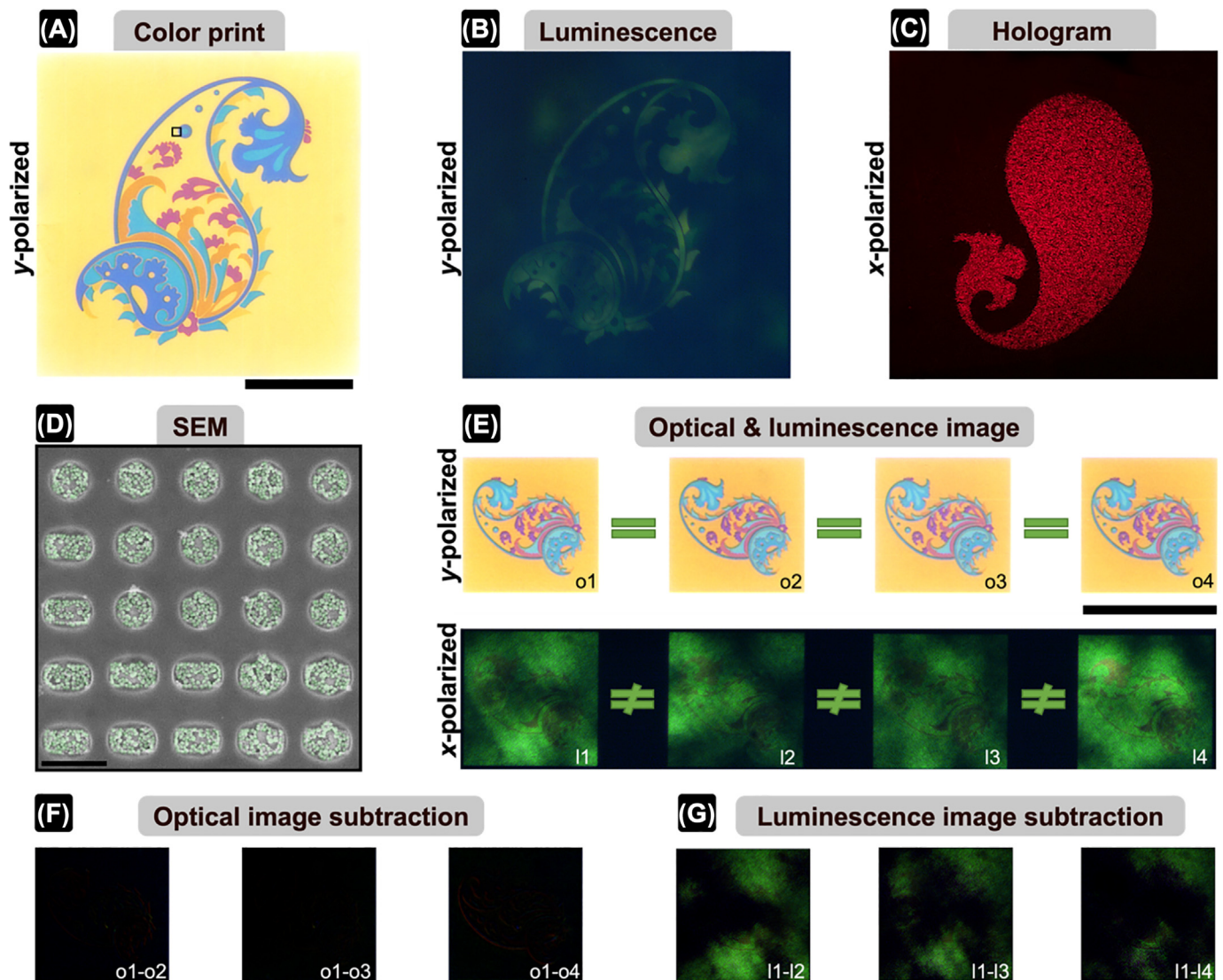


FIGURE 5

(A) Optical image of the tri-functional metasurface under y -polarized white light source. (B) Luminescence image of the same metasurface under y -polarized near-infrared excitation of 980 nm. (C) The reflected holographic image captured in the far-field when the sample is illuminated with an x -polarized red laser beam at 638 nm. (D) False colorized SEM image of the area with UCNPs highlighted in panel (A) before deposition of SiO_2 and Al capping layers. (E) Optical and luminescence image of samples with nominally identical EBL exposure and process conditions under y -polarized white source (top) and x -polarized near-infrared excitation of 980 nm (bottom). (F) Image analysis displaying subtraction of optical images in (E). (G) Image analysis displaying subtraction of luminescence images in (E). The scale bars in (A), (D) and (E) are 100 μm , 200 nm, and 150 μm respectively.

various polarizations (Fig. S12) which is consistent with results in Fig. 4.

It should be highlighted that the luminescent image in Fig. 5B is correlated with the color print in Fig. 5A. However, the presence of the luminescent feature would make any counterfeiting effort significantly more difficult as all features are incorporated into a single metasurface. The SEM image in Fig. 5D further depicts the UCNPs in the sample before deposition of capping layers. The distribution nearly covers the exposed surface of the pattern, although it is not entirely uniform. This random distribution of the UCNPs generates a unique “fingerprint”, achieving a physically unclonable function (PUF) layer, further enhancing the security of the metasurface.

While the optical images of samples with nominally identical EBL exposures and process conditions are nearly the same as elucidated in Fig. 5E top, due to the stochastic distribution of UCNPs, no two luminescence images can be identical (Fig. 5E bottom). In order to quantify the identity and the difference of the optical and luminescence images in Fig. 5E, image subtraction was performed. Fig. 5F illustrates optical images o2 to o4 subtracted from optical image o1. As can be seen the subtraction images appear black *i.e.*, the image difference is approximately zero. This identity is clear from o1 to o4 optical images as they closely resemble one another. However, by examining the luminescence image subtractions l1-l2, l1-l3, and l1-l4 in Fig. 5G, the actual difference between the luminescence images in Fig. 5E is revealed. As observed, luminescence images l1 to l4 are drastically different due to the stochastic distribution of the UCNPs. This difference is also observed for luminescence images of the same samples in Fig. 5E under γ -polarized NIR laser (Fig. S13). To utilize the PUF feature in a practical application, the lumines-

cence image of each fabricated metasurface could be imaged and recorded in a database. The stochastic distribution of the UCNPs imparts unique luminescence images. During authentication, the luminescence image would be scanned and cross-checked with the database through image analysis. As each metasurface is unique, any attempt of counterfeiting would be revealed.

The field of metasurface-driven optically variable devices (mOVDs) has recently received growing attention. Table 1 compares the latest research efforts in terms of the main optical channels, *i.e.*, amplitude, phase, and luminescence, with present work. Thus far, various optical designs, including high/low-index dielectrics, plasmonic, and Fabry-Pérot have been employed to generate color images and holograms through amplitude and phase control. These designs work in reflection, transmission, or a combination of both. Moreover, the light/laser source often needs to possess a particular polarization state for the metasurface to accurately display the encoded information. It is worth highlighting that several attempts have been made to utilize dynamic metasurfaces that employ active materials such as liquid crystals (LC) for optical anticounterfeiting and encryption, highlighted in this comparison [63–65].

In addition to multiple functions and security layers, easy authentication is crucial for end-user in practical applications. The color image and hologram can be easily revealed by a macro-lens and laser pointer without the need for a polarizer as demonstrated in Fig. S14, providing the overt and covert security features. While the luminescence adds a forensic security feature. Finally, our design facilitates adoption for many use case scenarios as it works in reflection mode, which is more desirable than transmission mode as many objects that need to be tagged are not transparent. It is worthwhile mentioning that various strate-

TABLE 1

Reported multifunctional metasurfaces to modulate amplitude, phase, and luminescence for anticounterfeiting application.

Report	Amplitude	Phase	Luminescence	Comments
Yoon et al. [36]	✓	✓	—	High-index dielectric; hologram in transmission; image in reflection
Lim et al. [38]	✓	✓	—	Low-index dielectric; operates in transmission; supports three holograms in the same print
Liu et al. [51]	✓	—	✓	Plasmonic; operates in reflection
Liu et al. [30]	✓	—	—	Plasmonic; operates in transmission; generates two distinct color images; requires circular polarization
Zhang et al. [46]	✓	✓	—	Plasmonic; operates in reflection
Hu et al. [40]	✓	✓	—	Low-index dielectric plus Fabry-Pérot; operates in transmission; full color hologram
Wen et al. [31]	✓	✓	—	High-index dielectric; operates in reflection; full color hologram
Bao et al. [34]	✓	✓	—	High-index dielectric; operates in transmission; full color hologram
Wei et al. [35]	✓	✓	—	High-index dielectric; operates in transmission; bi-color hologram; requires cross polarization for hologram
Zhang et al. [43]	✓	✓	—	Plasmonic; operates in reflection; full color hologram
Luo et al. [42]	✓	✓	—	Plasmonic plus Fabry-Pérot; image operates in reflection; full color hologram operates in transmission; hologram requires circular polarization
Li et al. [68]	✓	✓	—	Fabry-Pérot; operates in reflection; switchable between hologram and image mode by inducing H ₂ O ₂
Li et al. [65]	✓	—	—	Metallic/dielectric; operates in reflection; capable of generating multiple holograms by inducing H ₂ O ₂ . Requires circular polarization
Kim et al. [63]	✓	✓	—	High-index dielectric plus addressable liquid crystal (LC); dynamic metasurface; capable of generating multiple holograms by applying a voltage to the LC; requires analyzer for hologram
Zheng et al. [64]	✓	—	—	Metallic; operates in transmission; multiple image channels; can be used for computational imaging encryption
This work	✓	✓	✓	Plasmonic; operates in reflection; does not require polarized source or analyzer for color image and hologram

gies can be employed to extend this work to achieve multiple color holograms as previously reported in the literature [66]. Furthermore, it could be beneficial to completely decouple the observed color print from the luminescence image *e.g.*, by utilizing more complex nanostructures as displayed in Fig. S15. It would be possible to use machine learning to achieve same colors but different luminescence responses by identifying free-form nanostructures that have the same optical response in visible but different absorptance at the excitation wavelength in NIR [67].

Conclusions

In summary, we demonstrated simultaneous control of phase, amplitude, and luminescence by employing anisotropic gap-plasmon structures with upconversion nanoparticles incorporated in their dielectric gap. The tri-functional metasurface generated a color image under white light while producing a luminescence image under a near-infrared source and a hologram in the far-field by red laser illumination. Moreover, the stochastic distribution of the UCNPs in the metasurface creates a PUF feature. Therefore, the design presented here offers a nearly unclonable security tag by combining overt, covert, and forensic security features in addition to the PUF. Prior works heavily rely on complicated optical setups and various linear and nonlinear polarizations, while our approach overcomes these complications and offers simplicity in reading different channels through a macro-lens and a laser pointer. Our work paves the way for creating unclonable tags for easy authentication.

Materials and methods

Preparation of UCNPs: Ytterbium (III) acetate hydrate (99.9%), yttrium (III) acetate hydrate (99.9%), erbium (III) acetate hydrate (99.9%), oleic acid (90%), 1-octadecene (90%), sodium hydroxide (NaOH; >98%), ammonium fluoride (NH₄F; >98%) and cyclohexane were purchased from Sigma-Aldrich and used as received without further purification. NaYF₄:Yb/Er (18/2 mol%) nanocrystals were synthesized according to previous reports [69]. A 4-mL aqueous solution of Ln (CH₃CO₂)₃ (0.2 M, Ln = Y, Yb, and Er) was added to a 50-mL flask containing 6 mL of oleic acid and 14 mL of 1-octadecene. The reaction mixture was heated to 150 °C and kept for one h under stirring to remove water from the solution. After cooling to room temperature, a 12-mL methanol solution containing NH₄F (3.2 mmol) and NaOH (2 mmol) was added to the mixture and kept under stirring for 30 min. After removing the methanol, the solution was heated at 290 °C under argon for 1.5 h and then cooled to room temperature. The resulting nanoparticles were washed with ethanol several times and re-dispersed in 4 mL of cyclohexane.

Fabrication of Gap-Plasmon Structures: First, a 100-nm-thick Al film was deposited on Si wafer using electron beam evaporation (Kurt J. Lesker, deposition rate of 1 Å s⁻¹). The thickness and evaporation rates were measured *in situ* with a quartz balance. Second, poly-methyl methacrylate (PMMA A5, diluted in anisole solvent with ratio of 1:1) resist (950k molecular weight, 3.3% wt in anisole) was spin coated onto an Al-coated Si substrate at a spin speed of 3k revolutions-per-minute (rpm) to obtain a ~100 nm thick PMMA layer. The PMMA resist was then baked

at 180 °C for 120 s to remove the solvent. The sample was exposed by EBL (Elionix ELS-7000, electron acceleration voltage of 100 keV, beam current of 100 pA). Afterwards, the sample was developed in a solution of methyl isobutyl ketone (MIBK) and isopropyl alcohol (IPA) solution with a volume mixing ratio of 1:3, at a temperature of -10 °C for 15 s, followed by blow drying the sample with nitrogen.[70] Finally, 30-nm-thick SiO₂ and 40-nm-thick Al were deposited (with deposition rate of 1 Å s⁻¹), followed by a lift-off process (acetone at room temperature).

Fabrication of Gap-Plasmon Structures with UCNPs: First, a 100-nm-thick Al film was deposited on Si wafer using electron beam evaporation (Kurt J. Lesker, deposition rate of 1 Å s⁻¹). The thickness and evaporation rates were measured *in situ* with a quartz balance. Second, poly-methyl methacrylate (PMMA A5, diluted in anisole solvent with ratio of 1:1) resist (950k molecular weight, 3.3% wt in anisole) was spin coated onto an Al-coated Si substrate at a spin speed of 3k revolutions-per-minute (rpm) to obtain a ~100 nm thick PMMA layer. The PMMA resist was then baked at 180 °C for 120 s to remove the solvent. The sample was exposed by EBL (Elionix ELS-7000, electron acceleration voltage of 100 keV, beam current of 100 pA). Afterwards, the sample was developed in a solution of methyl isobutyl ketone (MIBK) and isopropyl alcohol (IPA) solution with a volume mixing ratio of 1:3, at a temperature of -10 °C for 15 s, followed by blow drying the sample with nitrogen. Next, the UCNPs water solution was spin coated onto the sample at a spin speed of 5k revolutions-per-minute (rpm) and baked at 90 °C for 1 min. In the end, 7.5-nm-thick SiO₂ and 40-nm-thick Al were deposited (with deposition rate of 1 Å s⁻¹), followed by a lift-off process (acetone at room temperature).

SEM Characterization: The SEM images were obtained using the eLINE Plus system (Raith) at an acceleration voltage of 10 kV and an aperture size of 30 μm.

Optical Characterization: Reflectance spectra were measured with a micro-spectrophotometer (CRAIC) equipped with a 20 × lens (NA = 0.45). The reflectivity of a 100-nm-thick Al mirror was measured as the reference signal. All the optical microscopy images were collected with the same microscope system.

Upconversion Luminescence Imaging: Upconversion luminescence microscopy images were collected on an Olympus BX51 microscope with a Xenon lamp adapted to a 980 nm CW laser and equipped with a 20 × lens (NA = 0.45). The excitation power was set to 60 mW. and images were scanned with a 1 s integration time.

Hologram Design: The binary hologram was designed by computer-generated hologram with an adaptive Fourier transform based algorithm. The Gerchberg-Saxton algorithm was adopted to get the final binary phase [71]. First, a plane wave (laser) passed through a random phase and a projection was obtained in the far-field; Second, the amplitude of the projection was replaced by the designed image and then inverse Fourier transform was performed; Third, in the hologram plane, the amplitude was replaced by the plane wave and then Fourier transform was carried out again. The signal to noise ratio stabilized after iterations and the phase was limited to be binary to fit in our design.

Photography of Holographic Projections: Holograms were projected in reflection onto a white screen and photographed using

a DSLR camera in a darkened room. Coherent illumination was provided by 638 nm red laser diode module with a maximum power of 4.5 mW (ThorLabs). The distance of the holographic colour prints from the screen (projection distance) was 30 cm, at which the holographic projections measured between 10 and 15 cm across.

Numerical Simulations: Finite-difference time-domain simulations were carried out using a commercial software (Lumerical FDTD Solutions). To calculate the electric field and power loss map, a standard plane wave was employed with periodic boundary conditions along the x - and y -axes. Due to structural symmetry, symmetry conditions were used to reduce the computational time. Perfectly matched layers were used along the propagation direction at the top and bottom boundaries. The permittivity data of Al and SiO₂ were obtained from the literature [72].

Image Analysis: The image subtraction was carried out by the image analysis software ImageJ.

CRedit authorship contribution statement

Soroosh Daqiqeh Rezaei: Conceptualization, Methodology, Software, Validation, Formal analysis, Investigation, Data curation, Writing – original draft, Visualization, Funding acquisition. **Zhaogang Dong:** Conceptualization, Methodology, Investigation, Writing – review & editing, Resources, Funding acquisition. **Hao Wang:** Methodology, Investigation, Software, Writing – review & editing. **Jiahui Xu:** Investigation, Writing – review & editing. **Hongtao Wang:** Investigation, Writing – review & editing. **Mohammad Tavakkoli Yaraki:** Methodology, Writing – review & editing. **Ken Choon Hwa Goh:** Investigation, Writing – review & editing. **Wang Zhang:** Investigation, Writing – review & editing. **Shaban Reza Ghorbani:** Methodology, Writing – review & editing. **Xiaogang Liu:** Methodology, Writing – review & editing. **Joel K.W. Yang:** Conceptualization, Resources, Writing – review & editing, Supervision, Project administration, Funding acquisition.

Data availability

Data will be made available on request.

Declaration of Competing Interest

The authors declare that they have no known competing financial interests or personal relationships that could have appeared to influence the work reported in this paper.

Acknowledgements

This research is supported by National Research Foundation (NRF) Singapore, under its Competitive Research Programme NRF-CRP001-021 and CRP20-2017-0004, as well as NRF Investigatorship Award NRF-NRFI06-2020-0005. In addition, Z.D. would like to acknowledge the funding support from A*STAR AME IRG grant (Project No. A20E5c0093), A*STAR CDA grant (Project No. C210112019) and A*STAR MTC IRG grant (Project No. M21K2c0116). J.K.W.Y. and S.D.R. would like to acknowledge the Decentralized Gap Funding.

Data and materials availability

All data are available in the manuscript and the supporting materials.

Appendix A. Supplementary material

Supplementary data to this article can be found online at <https://doi.org/10.1016/j.mattod.2022.11.010>.

References

- [1] S. Daqiqeh Rezaei et al., ACS Photonics 8 (2021) 18–33.
- [2] A. Kristensen et al., Nat. Rev. Mater. 2 (2016) 1–14.
- [3] S. Daqiqeh Rezaei et al., Nano Lett. 20 (2020) 4422–4429.
- [4] S. Daqiqeh Rezaei et al., Opt. Mater. 7 (2019) 1900735.
- [5] X. Cao et al., Adv. Mater. (2022) 2109161.
- [6] Z. Dong et al., Sci. Adv. 8 (2022) eabm4512.
- [7] Z. Dong et al., Nano Lett. 17 (2017) 7620–7628.
- [8] C. Shao et al., Mater. Today 51 (2021) 117–125.
- [9] M. Jiang et al., Mater. Today 35 (2020) 99–105.
- [10] J. Liao et al., Mater. Today 56 (2022) 29–41.
- [11] Z. Han et al., Sci. Adv. 8 (2022) 889.
- [12] S. Rossi et al., Adv. Mater. 33 (2021) 2105004.
- [13] M. Gugole et al., Nano Lett. 21 (2021) 4343–4350.
- [14] L. Huang et al., Adv. Mater. 27 (2015) 6444–6449.
- [15] S. Chen et al., Adv. Mater. 32 (2020) 1805912.
- [16] X. Zang et al., Adv. Mater. 30 (2018) 1707499.
- [17] H. Wang et al., Adv. Opt. Mater. 7 (2019) 1900068.
- [18] G. Zheng et al., Nat. Nanotechnol. 10 (2015) 308–312.
- [19] L. Jin et al., Nano Lett. 18 (2018) 8016–8024.
- [20] M. Khorasaninejad et al., Science 352 (2016) (1979) 1190–1194.
- [21] S. Wang et al., Nature Nanotechnol. 13:3 (2018) 227–232.
- [22] J. Engelberg, U. Levy, Nature Photonics 16:3 (2022) 171–173.
- [23] G. Cao et al., Mater. Today 50 (2021) 499–515.
- [24] J. Engelberg et al., Nanophotonics 9 (2020) 361–370.
- [25] J. Deng et al., Nano Lett. 20 (2020) 1830–1838.
- [26] Z. Xu et al., Nano Lett. 21 (2021) 5269–5276.
- [27] C. Zhang et al., Phys. Rev. Appl. 10 (2018) 34028.
- [28] C. Zhang et al., Phys. Rev. Appl. 12 (2019) 34028.
- [29] Z. Li et al., Adv. Mater. 32 (2020) 1907983.
- [30] H.L. Liu et al., Nanoscale 11 (2019) 5506–5511.
- [31] D. Wen et al., Adv. Funct. Mater. 30 (2020) 1906415.
- [32] C. Jung et al., Chem. Rev. 121 (2021) 13013–13050.
- [33] R. Arppe, T.J. Sørensen, Nat. Rev. Chem. 1 (2017) 1–13.
- [34] Y. Bao et al., Light Sci. Appl. 8 (2019).
- [35] Q. Wei et al., Nano Lett. 19 (2019) 8964–8971.
- [36] G. Yoon et al., ACS Nano 12 (2018) 6421–6428.
- [37] Z. Li et al., Laser Photon Rev. 14 (2020) 2000032.
- [38] K.T.P. Lim et al., Nat. Commun. 10 (2019) 1–8.
- [39] H. Wang et al., Nano Lett. 21 (2021) 4721–4729.
- [40] Y. Hu et al., Light Sci. Appl. 8 (2019) 1–9.
- [41] I.-H. Lee et al., Opt. Express 27 (2019) 24512.
- [42] X. Luo et al., Adv. Opt. Mater. 8 (2020).
- [43] F. Zhang et al., Adv. Sci. 7 (2020) 1903156.
- [44] S. Boroviks et al., ArXiv Preprint ArXiv:2111.07561 (2021).
- [45] R. Deshpande et al., Nano Lett. 18 (2018) 6265–6270.
- [46] Y. Zhang et al., Nanoscale Horiz. 4 (2019) 601–609.
- [47] A. Pors, S.I. Bozhevolnyi, Opt. Express 21 (2013) 27438–27451.
- [48] C. Damgaard-Carstensen et al., Sci. Rep. 10 (2020) 1–11.
- [49] A.S. Roberts et al., Nano Lett. 14 (2014) 783–787.
- [50] M. Miyata, H. Hatada, J. Takahara, Nano Lett. 16 (2016) 3166–3172.
- [51] H. Liu et al., Adv. Mater. 31 (2019) 1807900.
- [52] Y. Deng et al., ACS Nano 15 (2021) 18532–18540.
- [53] Z. Cai et al., Adv. Opt. Mater. 9 (2021) 2002253.
- [54] F. Ding, Y. Chen, S.I. Bozhevolnyi, Photonics Res. 8 (2020) 707–714.
- [55] R. Feng et al., Adv. Funct. Mater. 32 (2022) 2108437.
- [56] S. Boroviks et al., Opt. Mater. Express 9 (2019) 4209–4217.
- [57] R.A. Deshpande, F. Ding, S. Bozhevolnyi, ACS Appl. Mater. Interfaces 12 (2019) 1250–1256.
- [58] A. Pors et al., Sci. Rep. 3 (2013) 1–6.
- [59] C. Meng et al., ACS Photonics 7 (2020) 1849–1856.
- [60] S.D. Rezaei et al., ACS Nano 13 (2019) 3580–3588.
- [61] S.D. Rezaei et al., Opt. Express 25 (2017) 27652–27664.
- [62] J.J. Baumberg et al., Nat. Mater. 18 (2019) 668–678.
- [63] I. Kim et al., Nat. Commun. 12 (2021) 1–9.
- [64] P. Zheng et al., Sci. Adv. 7 (2021) eabg0363.
- [65] J. Li et al., Sci. Adv. 4 (2018) eaar6768.

- [66] Y.W. Huang et al., *Nano Lett.* 15 (2015) 3122–3127.
- [67] J. Trisno et al., *Adv. Photonics Res.* (2020) 2000068.
- [68] J. Li et al., *ACS Nano* (2020), <https://doi.org/10.1021/acsnano.0c01469>.
- [69] X. Xie et al., *J. Am. Chem. Soc.* 135 (2013) 12608–12611.
- [70] Z. Dong et al., *Nanotechnology* 25 (2014) 135303.
- [71] R.W. Gerchberg, W.O. Saxton, *Optik (Stuttgart)* 35 (1972) 237–250.
- [72] E.D. Palik, *Handbook of Optical Constants of Solids*, Academic Press, New York, 1998.